Canadian Science Publishing | Transactions of the Canadian Society for Mechanical Engineering

Contact simulation analysis of double cylindrical asperities based on finite element method

Journal:	*Transactions of the Canadian Society for Mechanical Engineering*
Manuscript ID	TCSME-2018-0186.R1
Manuscript Type:	Article
Date Submitted by the Author:	20-Jan-2019
Complete List of Authors:	Wang, Lihua; Kunming University of Science & Technology, Faculty of Mechanical & Electrical Engineering Chen, Liheng; Kunming University of Science & Technology, Faculty of Mechanical & Electrical Engineering Huang, Yayu; Kunming University of Science & Technology, Faculty of Mechanical & Electrical Engineering Yao, Tingqiang; Kunming University of Science & Technology Wang, Chunfeng; Kunming University of Science & Technology, Faculty of Mechanical & Electrical Engineering
Keywords:	cylindrical asperity, contact characteristics, elastoplastic contact, finite element
Is the invited manuscript for consideration in a Special Issue? :	Not applicable (regular submission)

A novel fault diagnosis method based on improved adaptive VMD energy entropy and PNN

Shengjie Zhang[1,2], Huimin Zhao[1,3], Junjie Xu[1], Wu Deng[1,3,4]*

[1]*College of Electronic Information and Automation, Civil Aviation University of China, Tianjin 300300, China*
[2]*School of Electronics and Information Engineering, Dalian Jiaotong University, Dalian, 116028 China*
[3]*The State Key Laboratory of Mechanical Transmissions, Chongqing University, Chongqing 400044, China*
[4]*Traction Power State Key Laboratory of Southwest Jiaotong University, Chengdu 610031 China*

* *Corresponding author. E-mail address: dw7689@163.com*

Abstract

In order to improve the accuracy of bearing fault recognition, a novel bearing fault diagnosis(PAVMD-EE-PNN) method based on parametric adaptive Variational Mode Decomposition (VMD) energy entropy and Probabilistic Neural Network (PNN) is proposed in this paper. In view of the effect of VMD on signal decomposition effect affected by the number of preset modes decomposition, a central frequency screening method is proposed to determine the number of decomposition modes of the VMD method. The parametric adaptive VMD method is used to decompose the bearing fault signal into a series of IMF components. The energy entropy of IMF components is calculated to form an eigenvector, which is input into the PNN model for training in order to obtain a fault recognition model with maximum output probability. The actual bearing vibration data is obtained and used to test and verify the effectiveness of the PAVMD-EE-PNN method. The experimental results show that the PAVMD-EE-PNN method can effectively and accurately identify the fault type, and the fault recognition effect is better than the contrast fault diagnosis methods.

Keywords: Variational mode decomposition; Signal decomposition; Central frequency screening;Energy entropy; Probabilistic neural network;Fault diagnosis

1. Introduction

Rolling bearing is an important part of motor. Its running state determines the working state of motor (Shen et al.2013; Wen et al.2019; Qian et al.2019; Luo et al.2018). Bearing is easy to be damaged during motor running. According to data statistics, 70% of mechanical faults are vibration faults, and about 30% of vibration faults are caused by rolling bearing faults (Zhang et al. 2018; Deng et al. 2019a; Ren et al. 2019a; Abdelkader et al. 2018; Zhao et al. 2018; Zhang et al. 2018; Zhou et al. 2019; Kanget al. 2018; Yual. 2018; Chen et al. 2019). Therefore, the effective analysis and accurate diagnosis of motor bearing faults have very important scientific significance and application value.

When the bearing fault occurs, the vibration signal in the running process contains important fault information. How to extract the fault information effectively becomes the key part of fault diagnosis (Li et al. 2017; Deng et al. 2019b; Zhu et al. 2019; Zhou et al. 2018a; Yang et al. 2018; Lu et al. 2018; Zhao et al. 2017; Chen et al. 2019; Deng et al. 2017a; Cai et al. 2019; Wu et al. 2019). At present, the most commonly used method for bearing fault diagnosis is to extract the fault features from the bearing vibration signal, and to realize the fault diagnosis by using the pattern recognition method (Zhang et al. 2017; Su et al. 2019; Shen et al. 2016; Song et al. 2019; Zhang et al. 2018; Lin et al. 2018; Liu et al. 2018; Cai et al. 2018; Peng et al. 2017; Huang et al. 2018; Guo et al. 2018a; Wen et al. 2019a; Fu et al. 2018; Yu et al. 2018;). In view of the nonlinear and non-stationary characteristics of vibration signals, some achievements have been achieved in bearing fault diagnosis by using traditional time-frequency analysis methods, such as short-time Fourier transform, wavelet transform and so on (Wen et al. 2019b; Liu et al. 2019a; Deng et al. 2017b; Guo et al. 2019; Yang et al. 2018; Liu et al. 2019b; Ren et al. 2019b; Cao et al. 2019; Guo et al. 2018b; Sun et al. 2017; Xu et al. 2019). Dong et al. (2009) proposed a novel method that can improve the sifting process's efficiency. Gong and Qiao (2013) proposed a method consisting of appropriate current frequency and amplitude demodulation algorithms for bearing fault diagnosis. Jiang et al. (2014) proposed a new fault diagnosis approach based on probabilistic PCA and cyclic bispectrum. Chen et al. (2015) proposed a new double-dot structuring element for multi-scale mathematical morphology. Wang et al. (2017) proposed a novel multiscale filtering spectrum method to obtain the weighted energy distribution of the monocomponent signals. Lu et al. (2019a) proposed a full-wave signal construction strategy for enhancing rotating machine fault diagnosis. Lu et al. (2019b) proposed a novel fast and online fault diagnosis method to realize variable-speed permanent magnet synchronous motor bearing. Deng et al. (2018) proposed a novel fault diagnosis method based on integrating empirical wavelet transform and fuzzy entropy. Yu and He (2018) proposed a fault diagnosis method of planetary gearboxes based on data-driven valued characteristic multigranulation model.

The VMD is a new adaptive signal analysis method, in which the frequency center and bandwidth of each component are determined by iterative search for the optimal solution of the variational model (Dragomiretskiy and Zosso 2014). Therefore, the frequency domain division of the signal and the effective separation of each component can be realized adaptively. When VMD is used to decompose signal, the number of mode decomposition must be preset, and the decomposition effect is affected by the number of decomposition components (Lian et al. 2018; Duan et al. 2018; Xie et al. 2019; Zhang et al. 2016; Fu et al. 2019; Zhou et al. 2018b; Chen et al. 2018). Zhu et al. (2017) proposed an adaptive VMD method with parameter optimization for detecting the localized faults. Wang et al. (2017) proposed a hybrid approach to fault diagnosis of bearings under variable speed conditions. Wan et al. (2018) proposed an improved fast spectrum kurtosis method combined with the VMD. Mohanty et al. (2018) proposed a novel fault identification method using correlation coefficient and Hurst exponent to depict the actual fault mode. Wang et al. (2018) proposed a novel PSO-VMD method, which adopts the minimum mean envelope entropy to optimize the parameters (α and K). Yu et al. (2019) proposed a fault severity identification method using flow graph and non-naive Bayesian inference for roller bearings.

In this paper, a novel bearing fault diagnosis method based on parametric adaptive VMD, energy entropy and PNN is proposed. Firstly, a central frequency screening method is proposed, in which the minimum value of the standard deviation of the central frequency is taken as the evaluation parameter to determine the number of modal decomposition adaptively. Then a series of IMF components are obtained by decomposing the signal with improved VMD, and then the eigenvector is constructed by solving the energy entropy of IMF component. Finally, the eigenvector is input into the PNN training model, and the bearing fault diagnosis is realized in the form of the maximum output probability.

2. Methodology

2.1. Variational mode decomposition

VMD is a completely non-recursive signal decomposition method, its essence is multiple Wiener filter banks (Dragomiretskiy and Zosso 2014). The constructed variational model can solve the noise in the signal. The Wiener filtering algorithm can effectively remove the noise from the signal. It shows that the method has good performance in dealing with noise and has better noise robustness. The VMD decomposes the signal into a number of discrete sparse sub-signals, that is, the Intrinsic Mode Function(IMF). Assuming that each mode u_k has center frequency $\omega(k)$ and linited bandwidth, the constraint condition is that the sum of each mode is equal to the input signal, and the sum of estimated bandwidth of each mode is the minimum. The $\omega(k)$ and bandwidth of each mode are updated continuously during the iterative process of solving the variational model, and finally the adaptive decomposition of the signal is realized.

The signal is decomposed at scale K and the variational problem is constructed with the minimum of the sum of the estimated bandwidths of the IMF components.

$$\min_{\{u_k\},\{\omega_k\}} \left\{ \sum_k \left\| \partial_t \left[\left(\delta(t) + \frac{j}{\pi t} \right) * u_k(t) \right] e^{-j\omega_k t} \right\|_2^2 \right\} \quad (1)$$

Where $\{u_k\} = \{u_1, u_2, ..., u_K\}$ represents each modal function and $\{\omega_k\} = \{\omega_1, \omega_2, ..., \omega_K\}$ represents the central frequencies of each modal function.

In order to transform the constraint problem into an unconstrained problem, the quadratic penalty factor and Lagrange multiplier are introduced. The quadratic penalty factor is used to guarantee the fidelity of the reconstructed signal, and the Lagrange multiplier is used to guarantee the strictness of the constraint. The extended Lagrange expression is as follows:

$$L(\{u_k\},\{\omega_k\},\lambda) = \alpha \sum_k \left\| \partial_t \left[\left(\delta(t) + \frac{j}{\pi t} \right) * u_k(t) \right] e^{-j\omega_k t} \right\|_2^2 + \left\| f(t) - \sum_k u_k(t) \right\|_2^2 + \left\langle \lambda(t), f(t) - \sum_k u_k(t) \right\rangle \quad (2)$$

where, α represents a penalty factor; λ represents a Lagrangian multiplier.

In VMD, the multiplicative operator alternating direction method is used to solve thee variational problems. By alternately updating u_k^{n+1}, ω_k^{n+1} and λ, we seek the "saddle point" of the extended Lagrangian expression. The modal component u_k and the center frequency ω_k are described as follows.

$$\hat{u}_k^{n+1}(\omega) = \left(\hat{f}(\omega) - \sum_{i \neq k} \hat{u}_i(\omega) + \frac{\hat{\lambda}(\omega)}{2} \right) \frac{1}{1 + 2\alpha(\omega - \omega_k)^2} \quad (3)$$

$$\omega_k^{n+1} = \frac{\int_0^\infty \omega |\hat{u}_k(\omega)|^2 d\omega}{\int_0^\infty |\hat{u}_k(\omega)|^2 d\omega} \quad (4)$$

where, $\hat{u}_k^{n+1}(\omega)$ is equivalent to the wiener filtering of the current residual $\hat{f}(\omega) - \sum_{i \neq k} \hat{u}_i(\omega)$ and the real part of $\hat{u}_k(\omega)$ after inverse Fourier transform is $u_k(t)$.

2.2. *Energy entropy*

The energy in the signal is distributed with the frequency. When the bearing fails, it will produce the corresponding fault frequency. In this case, the energy of the signal will change with the distribution of the frequency. The IMF component of the signal decomposed by VMD contains fault feature information. However, because of the narrow frequency domain range of the IMF component, it is easy to overlap in the frequency domain, which results in the difficulty of feature extraction. In order to accurately represent the change of the energy of the bearing fault signal with the frequency, The concept of energy entropy is introduced.

The original signal is decomposed by VMD to obtain K IMF components, and the energy E_1, E_2,...,E_k of the K IMF components are calculated. Because the decomposition result of VMD is orthogonal, the energy of each IMF component is the total energy of the original signal. E_1, E_2,...,E_k represents the energy of each IMF component of different frequency components in the original signal, thus the energy distribution of the original signal in the frequency domain is represented The corresponding energy entropy is defined as follows:

$$H_{EN} = -\sum_1^k p_i lg p_i \quad (5)$$

Where, $p_i = E_i / E$ represents the energy of the i-th IMF component as a percentage of the total energy.

2.3. Probabilistic neural networks

PNN is a new feedforward neural network. It overcomes the shortcoming of BP neural network which needs to calculate the reverse error. It has the advantages of less computation, stable results, strong fault tolerance and fast convergence rate and so on. The PNN contains input layer, pattern layer, summation layer and output layer. The basic constructure is shown in Fig.1.

(1) The input layer receives the sample eigenvector and passes it to the pattern layer. The number of neurons is equal to the dimension of the sample eigenvector.

(2) The pattern layer is connected to the input layer by connection weight value. The connection weight value is the matching degree between each neuron in the input layer and each neuron in the pattern layer. The formulas are described.

$$f(X, W_i) = exp \frac{-(X - W_i)^T (X - W_i)}{2\delta^2} \quad (6)$$

where, X represents the sample passed to the pattern layer, δ denotes the smoothing factor, and WCI represents the weight value between the input layer and the pattern layer.

(3) The summation layer calculates the probability of a certain category in the classification of samples, and then accumulates the probability, and obtains the probability density function of each pattern according to formula(7). The number of neurons is equal to the number of classification.

$$P(x|\omega_i) = \frac{1}{(2\pi)^{\frac{n}{2}} \delta^n N_i} \sum_{j=1}^{N_i} exp \frac{-(x - x_{ij})^T (x - x_{ij})}{2\delta^2} \quad (7)$$

where, x is the input sample of class ω_i, x_{ij} is the j-th sample of class ω_i, n is the dimension of sample eigenvector, and N_i is the sum of samples of class ω_i.

(4) The neurons of the output layer correspond to the class neurons in the summation layer, and the classification result is the output of the neuron corresponding to the maximum probability density of each category in the summation layer.

3. A novel bearing fault diagnosis(PAVMD-EE-PNN) method

3.1. Basic ideas of PAVMD-EE-PNN

At present, the commonly used fault diagnosis methods are wavelet transform, EMD, optimization algorithm, SVM, neural network, clustering analysis and so on. These methods have their own advantages and disadvantages in practical application. Because the VMD uses the non-recursive method in frequency domain, the signal decomposition accuracy is high and the mode aliasing can be avoided, but the number of modal decomposition must be preset. Energy entropy can accurately represent the variation of signal energy with frequency, and can accurately characterize the characteristics of the signal. PNN has the advantages that doesn't need to calculate reverse error, small computational complexity, stable results, fast convergence rate, and so on. It is a neural network commonly used in pattern classification. This paper applies the above method to fault diagnosis and presents a bearing fault diagnosis method based on parametric adaptive VMD energy entropy and PNN. In order to solve the problem that VMD needs to presuppose the number of modal decomposition, a method of center frequency selection is proposed. The improved VMD is used to decompose the signal, and a series of IMF components are obtained. By solving the energy entropy of the IMF component, the eigenvector of the training sample is input to the PNN for model training. The eigenvector of the test sample is inputted for fault diagnosis.

3.2. PAVMD-EE-PNN model

A fault diagnosis method based on parameter adaptive VMD energy entropy and PNN (PAVMD-EE-PNN) is proposed in this paper. The PAVMD-EE-PNN model is shown in Fig.2.

The detailed steps of fault diagnosis model are described as follows:

Step1. The vibration signal set is divided into training samples and test samples.

Step2. The number of mode decomposition of VMD is determined by the center frequency update screening method.

Step3. According to the K obtained from Step2, the training sample and test sample are decomposed by VMD, and some sets of IMF components are obtained.

Step4. The energy entropy of the IMF component obtained in the calculation Step3 constitutes the high-dimensional eigenvector of the training sample and the test sample.

Step5. The characteristic vector of the training sample is input to the PNN for model training.

Step6. The eigenvector of the test sample is input to PNN, to determine the bearing fault type according to the maximum probability of each kind of output, and the bearing fault diagnosis is realized.

3.3. Determination method of mode decomposition number of VMD

VMD decomposition needs to preset the number of mode decomposition K. How to effectively determine the number of decomposition will directly affect the final decomposition results. Therefore, the determination of K plays an important role in VMD. Each IMF component obtained by VMD decomposition corresponds to a central frequency, and the central frequency of IMF component in different scales is distributed from low to high. The distribution of central frequency varies with the increase of decomposition scale, and the center frequency is divided into low frequency band, middle frequency band and high frequency band. Standard deviation can reflect the dispersion degree of signal, the smaller the standard deviation is, the lower the signal dispersion is, that is, the stability of the signal is better. The standard deviation is used to weigh the central frequency distribution in a certain frequency band. If the signal is decomposed thoroughly at a certain scale, the sum of the standard deviation of the center frequency in the low frequency band, the middle frequency band and the high frequency band is the smallest. Determine K_{max} is the maximum scale of decomposition of VMD, decompose the signal at scales 2 to K_{max}, the central frequencies of each IMF component at different scales are obtained. The standard deviation of the center frequency in different frequency bands at different scales is solved respectively. If the standard deviation in a frequency band is all NaN, it shows that there is no signal component in this band. If the standard deviation in a frequency band exists NaN, it shows that there is no signal component in this band at the corresponding scale. If the standard deviation in a frequency band is all 0, it shows that the number of signal components in this band does not change with the increase of decomposition scale. By adding the standard deviations in different frequency bands at different scales, the minimum corresponding scale of the sum of standard deviations except 0 is the number of modal decomposition of VMD. If the standard deviations in a certain frequency band are all NaN, add up the standard deviations in other bands, the minimum corresponding scale of the sum of standard deviations except 0 is the number of modal decomposition of VMD.

The steps of improved VMD based on the central frequency screening method are described as follows:

Step1. Determine K_{max} is the maximum scale of decomposition of VMD;

Step2. The VMD is used to decompose the original signal, a series of IMF components at different scales are obtained, denoted as IMF_K. Calculate the central frequency of each component in the set IMF_K, denoted as $cf_{IMF_K}(K = 2,3,\ldots,K_{max})$;

Step3. Extract the center frequency of each frequency band in the set cf_{IMF_K} , denoted as $cf_{IMF_K}1$、$cf_{IMF_K}2$、$cf_{IMF_K}3$ $(K = 2,3,...,K_{max})$;

Step4. Calculate the standard deviation in the set $cf_{IMF_K}1$、$cf_{IMF_K}2$、$cf_{IMF_K}3$, denoted as $std^{cf}{}_{IMF_K}1$、$std^{cf}{}_{IMF_K}2$、$std^{cf}{}_{IMF_K}3(K = 2,3,...,K_{max})$;

Step5. Determine whether $std^{cf}{}_{IMF_K}1$、$std^{cf}{}_{IMF_K}2$、$std^{cf}{}_{IMF_K}3$ contains a set that is all NaN. If conditions are met, execute Step6; If not satisfied, execute Step7;

Step6. Calculate the sum of the sets that do not satisfy the judgment conditions in **Step5**, denoted as $0sumstd^{cf}{}_{IMF_K}$ $(K = 2,3,...,K_{max})$;

Step7. Calculate the sum of the sets $std^{cf}{}_{IMF_K}1$、$std^{cf}{}_{IMF_K}2$、$std^{cf}{}_{IMF_K}3$, denoted as $1sumstd^{cf}{}_{IMF_K}$ $(K = 2,3,...,K_{max})$;

Step8. Screen the minimum value other than 0 in the set $0sumstd^{cf}{}_{IMF_K}$ or $1sumstd^{cf}{}_{IMF_K}$, the scale K corresponding to the minimum value is the number of modal decomposition of VMD$(K = 2,3,...,K_{max})$.

4. Experimental results and analysis

4.1. Experimental data and environment

In order to verify the effectiveness of the proposed PAVMD-EE-PNN method, the QPZZ- Ⅱ rotary machinery test platform is used in here. The experimental platform can simulate many kinds of states and vibration of rotating machinery, can be compared, analyzed and diagnosed of various states, and can simulate the fault characteristics under different speed conditions. The range of transmission speed is 75-1450 rpm/min, the experimental platform is shown in Fig.3. In this paper, the single fault of normal, inner ring, outer ring and rolling body is selected to verify the method. In practical engineering, many faults often occur at the same time, so the next step is to solve the mixed fault problem with the method proposed in this paper. The mixed fault signal is decomposed by VMD to obtain the IMF component, the energy entropy of the IMF component is solved to form the eigenvector, and the eigenvector is input to the PNN, to identify the mixed fault.

In this paper, the USB-4431 data acquisition card produced by NI Company is used to collect the signal with LabVIEW. The speed of the motor is 1000r / min, the sampling frequency is 12kHz, the sampling time is 10s. By replacing the rolling bearing with different fault types, the normal signal and the inner ring, the outer ring and the rolling element fault signal under 0 load are collected, respectively. The main parameters of the VMD algorithm include the component number K, the penalty of factor alpha, and the fidelity tau. The number of components K directly affects the final decomposition result. The constraint problem to be solved is transformed the Lagrangian operator and the penalty factor alpha. The role of alpha is to improve the convergence. Through the simulation analysis, it can be seen that when there is noise amplitude is large, the strict data fidelity can be performed by changing tau to achieve accurate signal reconstruction. In the experiment, the signal is subjected to the VMD decomposition by changing the values of alpha and tau. It can be seen from the results that when alpha and tau are taken as default values, the good signal decomposition results can be obtained. Therefore, the initial value of the alpha is 2000 and the initial value of the tau is 0 in this paper. The experiment environments are: Matlab2014b, the Pentium CPU i7, 8.0GB RAM with Windows10.

The vibration signal samples collected in each state are divided into 50 sub-samples with data length of 2048 points, the total number of samples is 600, 90 samples in 4 states are selected to form training samples, and the other samples constituted test samples.

4.2. Determination of K value for VMD

Five samples are randomly selected from each type of state signal, a total of 20 samples, and the number of modal decompositions of VMD is determined by the method proposed in this paper. The results are shown in Tab.2.

It can be seen from Tab.2 that the determined K by the 5 normal samples is all 4, the determined K by 4 samples of the 5 inner ring fault samples is 6 and the determined K by the other one sample is 5, and the determined K by the 5 outer ring fault samples is all 4. The determined K by 5 rolling element fault samples is all 4, so the determined number of VMD modal decompositions of the normal and inner ring, outer ring and rolling element faults by the proposed method are 6, 4, 4 and 4 respectively. The improved VMD is used to decompose 600 samples and extract one sample of four state signals, respectively. The rolling element signal is selected in here. The time domain waveform is shown in Fig.4.

4.3. MD energy entropy

The energy entropy can accurately represent the variation of the energy of the fault signal with the frequency, so the energy entropy of the fault signal is solved as the fault feature in this paper. The energy entropy of each IMF component of 600 samples decomposed by VMD is solved, and the energy entropy of each sample is formed as the eigenvector of PNN. The calculated results are shown in Tab.3.

4.4. Results of fault diagnosis

The eigenvectors of the training samples and the test samples are input into the PNN network. The labels for the four working state samples of the normal and inner ring, outer ring and rolling element faults are 1, 2, 3, and 4 respectively, and the diagnosis results are shown in Fig.5.

It can be seen from table 4 that the recognition rates of the inner and outer ring samples are all 100%, the recognition rate of the rolling element samples is 96.677%, the recognition rate of the normal samples is 98.33%, the overall recognition rate is 98.75% and the overall operating time is 335.512s. It shows that the fault diagnosis method proposed in this paper can identify the fault type effectively and has high accuracy. Because VMD needs to presuppose the number of modal decomposition and the complexity of VMD itself, the overall running time is longer.

5. Comparison results and analysis

In order to verify the effectiveness of the improved VMD method proposed in this paper, the proposed method is compared with EMD energy entropy and PNN (EMD-EE-PNN), EEMD energy entropy and PNN (EEMD-EE-PNN). The diagnostic results are shown in Tab.5.

It can be seen from table 5 that the recognition rate of the PAVMD-EE-PNN method for four fault types is 100%. The recognition rate of outer ring fault by EMD-EE-PNN method is 100%, that of normal state is 86.67%, that of inner ring fault is 90% and that of rolling element fault is 63.33%. It can be seen that the EMD-EE-PNN method has the worst recognition effect for rolling element fault. The recognition rate of EEMD-EE-PNN is 100% for inner and outer ring faults, 93.33% for normal state and 90% for rolling element fault. The average recognition accuracy is better than that of EMD-EE-PNN method. By comparing the recognition rate, the PAVMD-EE-PNN method has the highest recognition rate and the best recognition effect. From the running time, the PAVMD-EE-PNN method needs to presuppose the number of modal decomposition and the complexity of VMD itself, which leads to the long running time. The EEMD-EE-PNN method needs to add Gauss white noise many times because of EEMD decomposition. In this paper, the number of white noise is 100, which results in the long running time of EEMD method, the shortest running time of EMD-EE-PNN method. Combined with the recognition rate analysis, the PAVMD-EE-PNN method is superior to the other two methods.

To further verify the effectiveness of the PNN, compared with SVM and the diagnostic results are shown in Tab.6.

It can be seen from table 6 that the recognition rate of normal state, outer ring and rolling element fault by PAVMD-EE-SVM method is 100%, and that of inner ring fault is 95%. The recognition rate of outer ring fault by EMD-EE-SVM method is 100%, that of normal state is 70%, that of inner ring fault is 76.67% and that of rolling element fault is 81.67%. The recognition rate of outer ring fault by EEMD-EE-SVM method is 100%, that of normal state is 95%, that of inner ring fault is 83.33%, that of rolling element fault is 61.67%. The result shows that this method has the worst effect on rolling element fault recognition, and the overall recognition effect is better than that of EMD-EE-SVM method. By comparing the recognition rate, the PASVM-EE-SVM method has the highest recognition rate and the best recognition effect. From running time, the PAVMD-EE-PNN method needs to presuppose the number of modal decomposition and the complexity of VMD itself, which leads to the long overall running time. The EEMD-EE-PNN method needs to add Gauss white noise many times because of EEMD decomposition. In this paper, the number of white noise is 100, which results in the long running time of EEMD method and the shortest running time of EMD-EE-PNN method. Combined with the recognition rate analysis, the PAVMD-EE-SVM method is superior to the other two methods. It is proved that the classification effect of PNN is better than that of SVM.

By comparing the two methods of PAVMD-EE-PNN and PAVMD-EE-SVM, we can see that the fault recognition rate of PAVMD-EE-PNN method is higher than that of PAVMD-EE-SVM. The difference of running time between the two methods is about 0.1s. The recognition rate and running time show that the PAVMD-EE-PNN method proposed in this paper has the best effect on fault recognition, which proves the effectiveness of the proposed method.

6. Conclusion

In this paper, a novel bearing fault diagnosis based on parametric adaptive VMD energy entropy and PNN is proposed. Aiming at the problem that the effect of VMD decomposition signal is affected by the number of mode, so a center frequency screening method is proposed. It is used to realize the adaptive determination of the number of modal decomposition in VMD. After the signal is decomposed by VMD, a series of IMF components are obtained, and then the energy entropy of each IMF component is calculated. The eigenvector of the training sample is input to the PNN for training model, and the eigenvector of the test sample is input for fault diagnosis. The experimental results show that the central frequency screening method can effectively determine the mode number of VMD decomposition and has a higher decomposition accuracy. The proposed PAVMD-EE-PNN method can effectively identify the normal state and inner ring fault, outer ring fault and rolling element fault. The experiment comparison results show that the proposed PAVMD-EE-PNN method is better than EMD-EE-PNN, EEMD-EE-PNN, PAVMD-EE-SVM, EMD-EE-SVM, EEMD-EE-SVM.

Acknowledgments

The authors would like to thank all the reviewers for their constructive comments. This work was supported by the National Natural Science Foundation of China(51605068, 61771087, 51879027,51579024), the the Open Project Program of State Key Laboratory of Mechanical Transmissions of Chongqing University(SKLMT-KFKT-201803), Open Project Program of the Traction Power State Key Laboratory of Southwest Jiaotong University (TPL1705, TPL1803), and Liaoning BaiQianWan Talents Program. The program for the initialization, study, training, and simulation of the proposed algorithm in this article was written with the tool-box of MATLAB 2014b produced by the Math-Works, Inc.

References

Abdelkader, R., Kaddour, A., Derouiche, Z. 2018. Enhancement of rolling bearing fault diagnosis based on improvement of empirical mode decomposition denoising method. Int. J. Adv. Manuf. Tech., **97(5-8)**:3099-3117. doi:10.1007/s00170-018-2167-7.

Cai, W., Liu, C., Zhang, C., et al.2018. Developing the ecological compensation criterion of industrial solid waste based on emergy for sustainable development. Energy, **157**: 940-948. doi:10.1016/j.energy.2018.05.207.

Cai, W., Lai, K., Liu, C., et al. 2019. Promoting sustainability of manufacturing industry through the lean energy-saving and emission-reduction strategy. Sci. Total Environ., doi: 10.1016/j.scitotenv.2019.02.069.

Cao, B., Zhao, J.W., et al. 2019. 3D deployment optimization for heterogeneous directional wireless sensor networks on smart city. IEEE T. Ind. Inform., **15(3)**:1798-1808. doi: 10.1109/TII.2018.2884951.

Chen, H.L., Xu, Y.T., Wang, M.J., Zhao, X.H. 2019. A balanced whale optimization algorithm for constrained engineering design problems. Appl. Math. Model,**71**:45-59. doi: 10.1016/j.apm.2019.02.004.

Chen, Q., Chen, Z.W., Sun, W., Yang, G.A, Palazoglu, A., Ren, Z.Q. 2015. A new structuring element for multi-scale morphology analysis and its application in rolling element bearing fault diagnosis. J. Vib. Control, **21(4)**:765-789. doi:10.1177/1077546313486163.

Chen, R., Guo, S.K., Wang, X.Z., Zhang, T.L. 2019. Fusion of multi-RSMOTE with fuzzy integral to classify bug reports with an imbalanced distribution. IEEE T. Fuzzy Syst., doi: 10.1109/TFUZZ. 2019.2899809.

Chen, Z.L., Li, Z.N.2018.Fault diagnosis method of rotating machinery based on stacked denoising autoencoder.J. Intell. Fuzzy Syst.,**34(6)**:3443-3449. doi: 10.3233/JIFS-169524.

Deng, W., Yao, R., Zhao, H.M., Yang, X.H., Li, G.Y. 2019a. A novel intelligent diagnosis method using optimal LS-SVM with improved PSO algorithm. Soft Comput., **23(7)**, 2445-2462. doi: 10.1007/s00500-017-2940-9.

Deng, W., Xu, J.J., Zhao, H.M. 2019b. An improved ant colony optimization algorithm based on hybrid strategies for scheduling problem. IEEE Access, **7**, 20281-20292. doi: 10.1109/ACCESS.2019.2897580.

Deng, W., Zhao, H.M., Zou, L., Li, G.Y., Yang, X.H., Wu, D.Q. 2017a. A novel collaborative optimization algorithm in solving complex optimization problems. Soft Comput., **21(15)**, 4387-4398. doi:10.1007/s00500-016-2071-8.

Deng, W., Zhao, H.M., Yang, X.H., Xiong, J.X., Sun, M., Li, B. 2017b. Study on an improved adaptive PSO algorithm for solving multi-objective gate assignment. Appl. Soft Comput., **59**:288-302. doi:10.1016/j.asoc.2017.06.004.

Deng, W., Zhang, S.J., Zhao, H.M., Yang, X.H. 2018. A novel fault diagnosis method based on integrating empirical wavelet transform and fuzzy entropy for motor bearing. IEEE Access, **6(1)**:5042-35056. doi:10.1109/ACCESS.2018.2834540.

Dong, H.B., Qi, K.Y., Chen, X.F., Zi, Y.Y., He, Z.J., Li, B. 2009. Sifting process of EMD and its application in rolling element bearing fault diagnosis. J. Mech. Sci. Technol., **23(8)**:2000-2007. doi:10.1007/s12206-009-0438-9.

Duan, C.X., Li, F.E., Yang, M.H., Zhang H, Wu Y, Xi HX. 2018. Rapid synthesis of hierarchically structured multifunctional metal–organic zeolites with enhanced volatile organic compounds adsorption capacity. Ind. Eng. Chem. Res., **57**: 15385-15394. doi:10.1021/acs.iecr.8b04028.

Dragomiretskiy, K., Zosso, D. 2014. Variational mode decomposition. IEEE T. Signal Proces., **62(3)**:531-544. doi:10.1109/TSP.2013.2288675.

Fu, H., Manogaran, G., Wu, K., Cao, M., Jiang, S.,Yang, A.2019. Intelligent decision-making of online shopping behavior based on internet of things. Int. J. Inform. Manage., doi:10.1016/j.ijinfomgt.2019.03.010.

Fu, H., Li, Z., Liu, Z., Wang, Z. 2018. Research on big data digging of hot topics about recycled water use on micro-blog based on particle swarm optimization. Sustainability-Basel, **10**, 2488. doi:10.3390/su10072488.

Gong, X., Qiao, W. 2013. Bearing fault diagnosis for direct-drive wind turbines via current-demodulated signals. IEEE T Ind Electron, **60(8)**:3419-3428. 10.1109/TIE.2013.2238871.

Guo, J.H., Mu, Y., Xiong, M.D., Liu, Y.Q., Gu, J.X. 2019. Activity feature solving based on TF-IDF for activity recognition in smart homes. Complexity, doi: 10.1155/2019/5245373.

Guo, S.K., Liu, Y.Q., Chen, R., Sun, X., Wang, X.X. 2018a. Using an improved SMOTE algorithm to deal imbalanced activity classes in smart homes. Neural Processing Letters, doi:10.1007/s11063-018-9940-3.

Guo, S.K., Chen, R., Wei, M.M, Li, H., Liu, Y.Q. 2018b. Ensemble data reduction techniques and multi-RSMOTE via fuzzy integral for bug report classification. IEEE Access, **6**:5934-45950. doi:10.1109/ACCESS.2018.2865780.

Huang, D.S., Du, J.X. 2008. A constructive hybrid structure optimization methodology for radial basis probabilistic neural networks. IEEE T. Neural Networ., **19(12)**: 2099-2115. doi: 10.1109/TNN.2008.2004370.

Huang, F., Yao, C., Liu, W., Li, Y., Liu, X.2 018. Landslide susceptibility assessment in the Nantian area of China: A comparison of frequency ratio model and support vector machine. Geomat. Nat. Haz. Risk, **9(1)**: 919-938. doi:10.1080/19475705.2018.1482963.

Jiang, B.Z., Xiang, J.W., Wang, Y.X. 2014. Rolling bearing fault diagnosis approach using probabilistic principal component analysis denoising and cyclic bispectrum. J. Vib. Control, **22(10)**:2420-2433. doi:10.1177/1077546314547533.

Kang, L., Du, H.L., Du, X., Wang, H.T., Ma, W.L., Wang, M.L., Zhang, F.B.2018. Study on dye wastewater treatment of tunable conductivity solid-waste-based composite cementitious material catalyst. Desalin. Water Treat. **125**:296-301. doi: 10.5004/dwt.2018.22910.

Li, T.; Shi, J.; Li, X.; Wu, J.; Pan, F. 2019. Image encryption based on pixel-level diffusion with dynamic filtering and DNA-level permutation with 3D Latin cubes. Entropy, **21**, 319. doi:10.3390/e21030319.

Li, Z.N., Zhu, M., Chu, F.L.,He, X.P.2017.Adaptive radial sinc kernel distribution and its application in mechanical fault diagnosis. P. I. Mech. Eng. C-J. M. E. C.,231(3):485-493. doi: 10.1177/0954406215616985.

Lian, J.J., Liu, Z., Wang, H.J. 2018. Adaptive variational mode decomposition method for signal processing based on mode characteristic. Mech. Syst. Signal Pr., **107**: 53-77. doi:10.1016/j.ymssp.2018.01.019.

Liu, G., Chen, B., Gao, Z., Fu, H., Jiang, S., Wang, L., Yi, K. 2019a. Calculation of joint return period for connected edge data. Water, **11**, 300. doi:10.3390/w11020300.

Liu, G., Chen, B., Jiang, S,. Fu, H., Wang, L., Jiang, W. 2019b. Double entropy joint distribution function and its application in calculation of design wave height. Entropy, **21**, 64. doi:10.3390/e21010064.

Lin, J., Yuan, J.S. 2018. Analysis and simulation of capacitor-less reram-based stochastic neurons for the in-memory spiking neural network. IEEE T. Biomed Circ. S.,**12(5)**:1004-1017. doi:10.1109/TBCAS.2018.2843286.

Liu, Y.Q., Yi, X.K., Zhai, Z.G., Gu, J.X. 2018. Feature extraction based on information gain and sequential pattern for English question classification. IET Softw, **12(6)**:520-526. doi: 10.1049/iet-sen.2018.0006.

Lu, S.L., Qin, Y., Hang, J., Zhang, B.H., Wang, Q.J. 2019a. Adaptively estimating rotation speed from DC motor current ripple for order tracking and fault diagnosis. IEEE T. Instrum. Meas., **68**: 741-753. doi:10.1109/TIM.2018.2852978.

Lu, S.L., Zhou, P., Wang, XX, Liu YB, Liu F. 2018. Condition monitoring and fault diagnosis of motor bearings using undersampled vibration signals from a wireless sensor network. J. Sound Vib., **414**:81-96. doi:10.1016/j.jsv.2017.11.007.

Lu, S.L., Yan, R.Q., Liu, Y.B., Wang, Q.J. 2019b. Tacholess speed estimation in order tracking: A review with application to rotating machine fault diagnosis. EEE T. Instrum. Meas., doi:10.1109/TIM.2019.2902806.

Luo, J., Chen, H.L., Zhang, Q., Xu, Y.T., Huang, H., Zhao, X.H. 2018. An improved grasshopper optimization algorithm with application to financial stress prediction. Appl. Math. Model, **64**:654-668. doi: 10.1016/j.apm.2018.07.044.

Mohanty, S., Gupta, K.K., Raju, K.S. 2018. Hurst based vibro-acoustic feature extraction of bearing using EMD and VMD. Measurement,**117**:200-220. doi:10.1016/j.measurement.2017.12.012.

Peng, Y., Lu, B.L.2017. Discriminative extreme learning machine with supervised sparsity preserving for image classification. Neurocomputing, **261**: 242-252. doi:10.1016/j.neucom.2016.05.113.

Qian, G., Lu, S.L., Pan, D.H., Tang, H.S., et al. 2019. Edge computing: A promising framework for real-time fault diagnosis and dynamic control of rotating machines using multi-sensor data. IEEE Sens. J., doi: 10.1109/JSEN.2019.2899396.

Ren, Z.R., Skjetne, R., Jiang, Z.Y., Gao, Z., Verma, A.S. 2019a. Integrated GNSS/IMU hub motion estimator for offshore wind turbine blade installation. Mech. Syst. Signal Pr., 1**23**: 222-243. doi:10.1016/j.ymssp.2019.01.008.

Ren, Z.R., Skjetne, R., Gao, Z. 2019b. A crane overload protection controller for blade lifting operation based on model predictive control. Energies,**12(1)**, 50. doi: 10.3390/en12010050.

Shen, C.Q., He, Q.B., Kong, F. 2013. A fast and adaptive varying-scale morphological analysis method for rolling element bearing fault diagnosis. P. I. Mech. Eng C-J. M.E.C., **227**(6), 1362-1370. doi:10.1177/0954406212460628.

Shen, L., Chen, H.L., Yu, Z., Kang, W.C., et al. 2016. Evolving support vector machines using fruit fly optimization for medical data classification. Knowl-Based Syst., **96**:61-75. doi:10.1016/j.knosys.2016.01.002.

Song, J., Feng, Q., Wang, X., Fu, H., Jiang, W., Chen, B. 2019. Spatial association and effect evaluation of CO2 emission in the Chengdu-Qhongqing urban agglomeration: quantitative evidence from social network analysis. Sustainability-Basel, **11**, 1. doi:10.3390/su11010001.

Su, J., Sheng, Z.G., Xie, L.B., Li, G., Liu, A.X. 2019. Fast splitting based tag identification algorithm for anti-collision in UHF RFID system. IEEE T. Commun., **67(3)**:2527-2538. doi: 10.1109/TCOMM.2018.2884001.

Sun, F.R., Yao, Y.D., Chen, M.Q., Li, X.F., Zhao, L., Meng, Y., Sun, Z., Zhang, T., Feng, D. 2017. Performance analysis of superheated steam injection for heavy oil recovery and modeling of wellbore heat efficiency. Energy, **125**:795-804. doi:10.1016/j.energy.2017.02.114.

Sun, F.R., Yao, Y.D., Li, X.F. 2018. The heat and mass transfer characteristics of superheated steam coupled with non-condensing gases in horizontal wells with multi-point injection technique. Energy, **143**, 995-1005. doi:10.1016/j.energy.2017.11.028.

Wan, S.T., Zhang, X., Dou, L.J. 2018. Compound fault diagnosis of bearings using improved fast spectral kurtosis with VMD. J Mech Sci Technol, **32(11)**: 5189-5199. doi:10.1007/s12206-018-1017-8.

Wang J, Peng YY, Qiao W, Hudgins JL. 2017. Bearing fault diagnosis of direct-drive wind turbines using multiscale filtering spectrum. IEEE T. Ind. Appl., **53(3)**: 3029-3038. doi:10.1109/TIA.2017.2650142.

Wang, X.B., Yang, Z.X., Yan, X.A. 2018. Novel particle swarm optimization-based variational mode decomposition method for the fault diagnosis of complex rotating machinery. IEEE-ASME T. Mech., **23(1)**: 68-79. doi:10.1109/tmech.2017.2787686.

Wang, Y.X., Yang L., Xiang, J.W., Yang, J.W., He, S.L. 2017. A hybrid approach to fault diagnosis of roller bearings under variable speed conditions. Meas. Sci. Technol., **28(12)**,125104. doi:10.1088/1361-6501/aa9460.

Wen, J., Fang, X., Cui, J., et al. 2019a. Robust sparse linear discriminant analysis. IEEE T. Circ. Syst. Vid.,**29(2)**:390-403. doi: 10.1109/TCSVT.2018.2799214.

Wen, J., Han, N., Fang, X., et al. 2019b. Low-rank preserving projection via graph regularized reconstruction. IEEE T. Cybernetics, **49(4):**1279-1291. doi: 10.1109/TCYB.2018.2799862.

Wen, J., Zhong, Z.F., Zhang, Z., Fei, L.K., Lai, Z.H., Chen, R.Z. 2018. Adaptive locality preserving regression. IEEE T. Circ. Syst. Vid., doi:10.1109/TCSVT.2018.2889727.

Wu, J., Chen, Y., Zhou, T., Li, T.Y. 2019. An adaptive hybrid learning paradigm integrating CEEMD, ARIMA and SBL for crude oil price forecasting. Energies, **12**, 1239. doi:10.3390/en12071239.

Xie, H.M., Yang, K., Li, S.W., et al. 2019. Microwave heating-assisted pyrolysis of mercury from sludge. Mater Res Express, **6(1)**,015507. doi:10.1088/2053-1591/aae46b.

Xu, Y.T., Chen, H.L., Luo, J., Zhang, Q., Jiao, S., Zhang, X.Q.2019.Enhanced Moth-flame optimizer with mutation strategy for global optimization. Information Sciences, **492**:181-203. doi:10.1016/j.ins.2019.04.022.

Yang, A., Lim, S., Lin, H., Jin, D. 2018. Edge extraction of mineralogical phase based on fractal theory. Chaos Soliton Fract., **17**, 215-221. doi:10.1016/j.chaos.2018.09.028.

Yang, A.M., Yang, X.L., Chang, J.C., Bai, B., Kong, F.B., Ran, Q.B. 2018. Research on a fusion scheme of cellular network and wireless sensor networks for cyber physical social systems. IEEE Access, **6**:18786-18794. doi:10.1109/ACCESS.2018.2816565.

Yu, J., Ding, B., He, Y.J.2018. Rolling bearing fault diagnosis based on mean multigranulation decision-theoretic rough set and non-naive Bayesian classifier. J. Mech. Sci. Technol., **32(11)**:5201-5211. doi: 10.1007/s12206-018-1018-7.

Yu, W.J., Zeng, Z., Peng, B. ,et al. 2018. Multi-objective optimum design of high-speed backplane connector using particle swarm optimization. IEEE Access, **6(1)**, 35182-35193. doi:10.1109/ACCESS.2018.2847732.

Yu, J., He, Y.J. 2018. Planetary gearbox fault diagnosis based on data-driven valued characteristic multigranulation model with incomplete diagnostic information. J. Sound Vib., **429**: 63-77. doi:10.1016/j.jsv.2018.05.020.

Yu, J., Xu, Y.G., Yu, G.B., Liu, L.F. 2019. Fault severity identification of roller bearings using flow graph and non-naive Bayesian inference. P. I. Mech. Eng. C-J. M. E. C., doi: 10.1177/0954406219834966.

Zhang, F.Q., Wang, Z.W., Chang J., et al. 2017. A fast framework construction and visualization method for particle-based fluid. EURASIP J. Image Vide., **2017**,79. doi:10.1186/s13640-017-0227-9.

Zhang, F.Q., Lei, T.S., Li, J.H., et al. 2018. Real-time calibration and registration method for indoor scene with joint depth and color camera. Int. J. Pattern. Recogn., **2018**,1854021. doi:10.1142/S0218001418540216.

Zhang, Q., Chen, H.L., Luo, J., Xu, Y.T., et al. 2018. Chaos enhanced bacterial foraging optimization for global optimization. IEEE Access, **6(1)**, 64905-64919. doi: 10.1109/ACCESS.2018.2876996.

Zhang, Q., Jin, B., Wang, X., et al. 2018. The mono (catecholamine) derivatives as iron chelators: synthesis, solution thermodynamic stability and antioxidant properties research. Roy Soc. Open Sci., **5(6)**,171492. doi: 10.1098/rsos.171492.

Zhang, S.F., Wang, Y.X., He, S.L., Jiang, Z.S. 2016. Bearing fault diagnosis based on variational mode decomposition and total variation denoising. Meas. Sci. Technol., **27(7)**, 075101. doi:10.1088/0957-0233/27/7/075101.

Zhao, H.M., Sun, M., Deng, W., Yang, X.H. 2017. A new feature extraction method based on EEMD and multi-scale fuzzy entropy for motor bearing. Entropy, **19(1)**, 14. doi:10.3390/e19010014.

Zhao, H.M., Yao, R., Xu, L., Yuan, Y., Li, G.Y., Deng, W. 2018. Study on a novel fault damage degree identification method using high-order differential mathematical morphology gradient spectrum entropy. Entropy-Switz., **20(9)**, 682. doi:10.3390/e20090682.

Zhou, J.C., Du, Z.X., Liao, Y.H., Tang, A.H. 2018a. An optimization design of vehicle axle system based on multi-objective cooperative optimization algorithm . J. Chin. Inst. Eng., doi:10.1080/02533839. 2018.1534559.

Zhou, J.C., Gao, J.J., Wang, K.Z., Liao, Y.H. 2018b. Design optimization of a disc brake based on a multi-objective optimization algorithm and analytic hierarchy process method. T. Famena, **42(4)**:25-42. doi:10.21278/TOF.42403.

Zhou, Y.R., Li, T.Y., Shi, J.Y., Qian, Z.J. 2019. A CEEMDAN and XGBOOST–based approach to forecast crude oil prices. Complexity, Article ID 4392785. doi: 10.1155/2019/4392785.

Zhu, J., Wang, C., Hu, Z.Y., Kong, F.R., Liu, X.C. 2017. Adaptive variational mode decomposition based on artificial fish swarm algorithm for fault diagnosis of rolling bearings. P. I. Mech. Eng. C-J. M. E. C., **231(4)**:635-654. doi:10.1177/0954406215623311.

Zhu, Z.Y., Peng, G.L., Chen, Y.H., Gao, H.J. 2019. A convolutional neural network based on a capsule network with strong generalization for bearing fault diagnosis. Neurocomputing, **323**: 62-75. doi: 10.1016/j.neucom.2018.09.050.

Tab.1. Vibration signal sample

	Normal	Inner ring fault	Outer ring fault	Rolling element fault	Total sample
Training sample	90	90	90	90	360
Test sample	60	60	60	60	240
Sample label	1	2	3	4	

Tab.2. Determination of K value

Fault type	Label	$K=2$	$K=3$	$K=4$	$K=5$	$K=6$	$K=7$	K
Normal	1	NaN	0	45.49	153.40	172.46	168.58	4
	2	NaN	0	43.35	96.50	120.90	271.21	4
	3	NaN	0	36.04	125.49	161.16	183.13	4
	4	NaN	0	38.32	127.86	173.53	174.12	4
	5	NaN	0	44.64	86.90	93.08	132.95	4
Inner ring fault	1	NaN	NaN	NaN	NaN	128.40	167.06	6
	2	NaN	NaN	NaN	NaN	144.10	220.62	6
	3	NaN	NaN	NaN	83.17	140.37	223.23	5
	4	NaN	NaN	NaN	NaN	142.12	165.53	6
	1	NaN	NaN	NaN	NaN	128.40	167.06	6
Outer ring fault	1	NaN	0	151.90	194.90	176.54	170.67	4
	2	NaN	0	155.72	167.15	170.72	195.65	4
	3	NaN	0	153.13	164.91	155.93	184.15	4
	4	NaN	0	160.46	171.32	161.26	186.87	4
	5	NaN	0	157.26	169.14	160.84	186.09	4
Rolling element fault	1	NaN	0	28.06	114.21	176.95	207.79	4
	2	NaN	0	34.23	113.04	174.16	212.08	4
	3	NaN	0	34.40	146.52	184.90	186.23	4
	4	NaN	0	26.15	118.79	162.89	166.52	4
	5	NaN	0	29.55	107.50	134.79	148.64	4

Tab.3. Energy entropy of samples

Fault type	Label	IMF1	IMF2	IMF3	IMF4	IMF5	IMF6	Expected output
Normal	1	0.3649	0.3644	0.3204	0.1831			1
	2	0.3587	0.3351	0.3511	0.1692			1
	…	…	…	…	…			
	150	0.3374	0.3459	0.2940	0.1749			1
Inner ring fault	1	0.1943	0.3547	0.3597	0.2463	0.0754	0.1038	2
	2	0.1205	0.2549	0.3273	0.0634	0.0773	0.0996	2
	…	…	…	…	…	…	…	
	150	0.1526	0.3435	0.3678	0.0700	0.0930	0.1142	2
Outer ring fault	1	0.2620	0.1466	0.0558	0.0665			3
	2	0.2813	0.1562	0.0556	0.0557			3
	…	…	…	…	…			
	150	0.2750	0.1549	0.0568	0.0704			3
Rolling element fault	1	0.3664	0.2731	0.3654	0.2493			4
	2	0.3601	0.3361	0.3292	0.2494			4
	…	…	…	…	…			
	150	0.3424	0.2672	0.3212	0.2901			4

Tab.4. Fault diagnosis results

Fault type	Test sample	Correct recognition	Accuracy rate(%)	Running Time(s)	Average accuracy(%)
Normal	60	60	100	54.785	100%
Inner ring fault	60	60	100	161.001	

Outer ring fault	60	60	100	50.774
Rolling element fault	60	60	100	70.387

Tab.5. Comparison of fault diagnosis results with different methods

Method	Fault type	Test sample	Correct recognition	Accuracy rate(%)	Running Time(s)	Average accuracy(%)
EMD-EE-PNN	Normal	60	52	86.67	6.373	85
	Inner ring fault	60	54	90	6.885	
	Outer ring fault	60	60	100	7.17	
	Rolling element fault	60	38	63.33	6.296	
EEMD-EE-PNN	Normal	60	56	93.33	882.923	95.83
	Inner ring fault	60	60	100	897.027	
	Outer ring fault	60	60	100	834.035	
	Rolling element fault	60	54	90	924.965	
PAVMD-EE-PNN	Normal	60	60	100	54.785	100
	Inner ring fault	60	60	100	161.001	
	Outer ring fault	60	60	100	50.774	
	Rolling element fault	60	60	100	70.387	

Tab.6. Comparison results of fault diagnosis results with different methods

Method	Fault type	Test sample	Correct recognition	Accuracy rate(%)	Running Time(s)	Average accuracy(%)
EMD-EE-SVM	Normal	60	42	70	6.272	82.08
	Inner ring fault	60	46	76.67	6.784	
	Outer ring fault	60	60	100	7.069	
	Rolling element fault	60	49	81.67	6.195	
EEMD-EE-SVM	Normal	60	57	95	882.822	85
	Inner ring fault	60	50	83.33	896.926	
	Outer ring fault	60	60	100	833.934	
	Rolling element fault	60	37	61.67	924.864	
PAVMD-EE-SVM	Normal	60	60	100	54.684	98.75
	Inner ring fault	60	57	95	160.9	
	Outer ring fault	60	60	100	50.673	
	Rolling element fault	60	60	100	70.283	

Contact simulation analysis of double cylindrical asperities based on finite element method

Wang LiHua, Chen Liheng, Huang Yayu, Yao Tingqiang, Wang Chunfeng

Tables:

Tab. 1 Critical contact parameters of single cylindrical asperity

Critical contact parameters	Theoretical calculation value	Finite element calculation value	error /%
F_c/N	1.677	1.733	3.34
σ_{pc} /MPa	649.40	655.50	0.9
$a_c/\mu m$	1.64	1.76	7.3

Tab.2 The influence of the shape of the cylindrical micro convex bodies on contact characteristics in elastic contact stage

Δ \ δ^*	0.2	0.4	0.6	0.8	1.0
Δ_{1S}	0.0011	0.0115	0.0011	0.0042	0
Δ_{2S}	0.0620	0.0699	0.0901	0.1056	0.1163
$\Delta_{1\sigma}$	0.0112	0.0074	0.0015	0.0009	0.0015
$\Delta_{2\sigma}$	0.0530	0.0742	0.0915	0.1073	0.1287
Δ_{1a}	0.0051	0.0085	0.0026	0.0018	0.0033
Δ_{2a}	0.0422	0.0744	0.0976	0.1079	0.1360
Δ_{1F}	0.0096	0.0182	0.0216	0.0336	0.0117
Δ_{2F}	0.0382	0.0838	0.1349	0.177	0.2551

Tab.3 Statistical table of contact stress of double asperities with unequal peak distance (δ^*=0.1)

β	$S_{max}(MPa)$	Number of stress fields	Stress field blend	ξ_s	Interaction
0	95.54	1	—	—	—
0.1	78.58	2	No	0.82	Yes
0.2	86.15	2	No	0.90	Yes
0.6	95.51	2	No	0.99	No

Tab.4 Statistical table of contact stress of double asperities with different displacement loads (β=0.1)

σ_y (MPa)	δ	Stress field blend	η_s	ξ_s	Interaction
355	$0.1\delta_c$	No	0	0.85	Yes
	$0.3\delta_c$	No	0	0.86	Yes
	$0.5\delta_c$	No	0	0.87	Yes
	$0.7\delta_c$	No	0	0.87	Yes
	$0.9\delta_c$	Yes	0.08	0.86	Yes
1640	$4.0\delta_c$	Yes	0.26	0.85	Yes
	$8.0\delta_c$	Yes	0.33	0.84	Yes
	$12\delta_c$	Yes	0.33	0.83	Yes

Tab.5 Statistical table of contact strain of double asperities with unequal peak distance on different displacement loads

β	δ	Strain field blend	κ_U	ξ_s	Interaction
0.1	$0.1\delta_c$	Yes	0.58	0.85	Yes
	$0.3\delta_c$	Yes	0.61	0.86	Yes
	$0.5\delta_c$	Yes	0.65	0.87	Yes
0.2	$0.1\delta_c$	Yes	0.42	0.90	Yes
	$0.3\delta_c$	Yes	0.51	0.92	Yes
	$0.5\delta_c$	Yes	0.49	0.91	Yes
0.6	$0.1\delta_c$	Yes	0.17	0.99	No
	$0.3\delta_c$	Yes	0.18	0.99	No
	$0.5\delta_c$	Yes	0.19	0.99	No

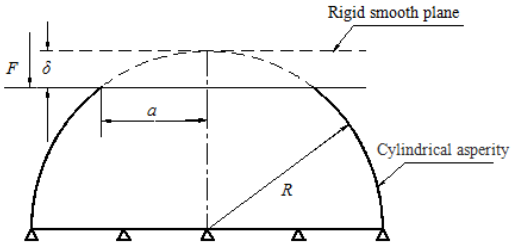

Figure 1: *Contact model of single cylindrical asperity and rigid plane*

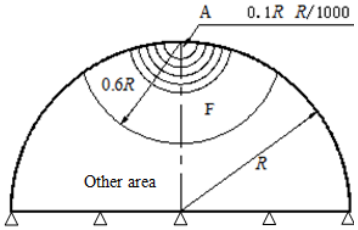

Area	R_b	Element size
A	0.1*R*	*R*/1000
B	0.15*R*	*R*/500
C	0.2*R*	*R*/250
D	0.25*R*	*R*/125
E	0.3*R*	*R*/62
F	0.6*R*	*R*/30
Other		*R*/20

Figure 2: *Element mesh partition and size setting*

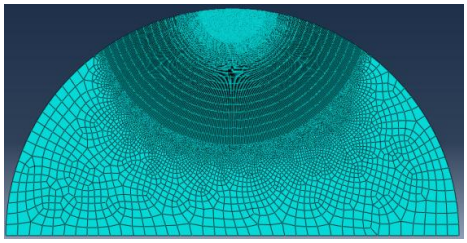

***Figure 3**: Finite element mesh of single cylindrical asperity*

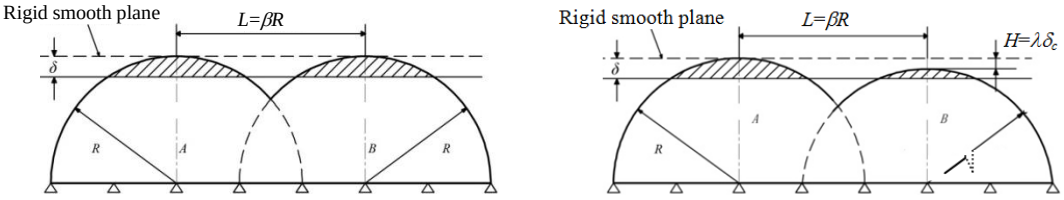

(a) Equal height double cylindrical asperities (b) Unequal height double cylindrical asperities

Figure 4: *Contact model of double cylindrical asperities*

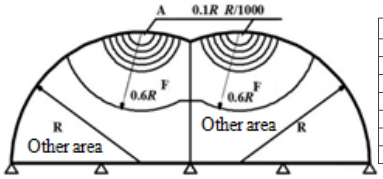

Area	R_b	Element size
A	0.1*R*	*R*/1000
B	0.15*R*	*R*/500
C	0.2*R*	*R*/250
D	0.25*R*	*R*/125
E	0.3*R*	*R*/62
F	0.6*R*	*R*/30
Other		*R*/20

Figure 5: *Element mesh partition and size setting of double cylindrical asperities*

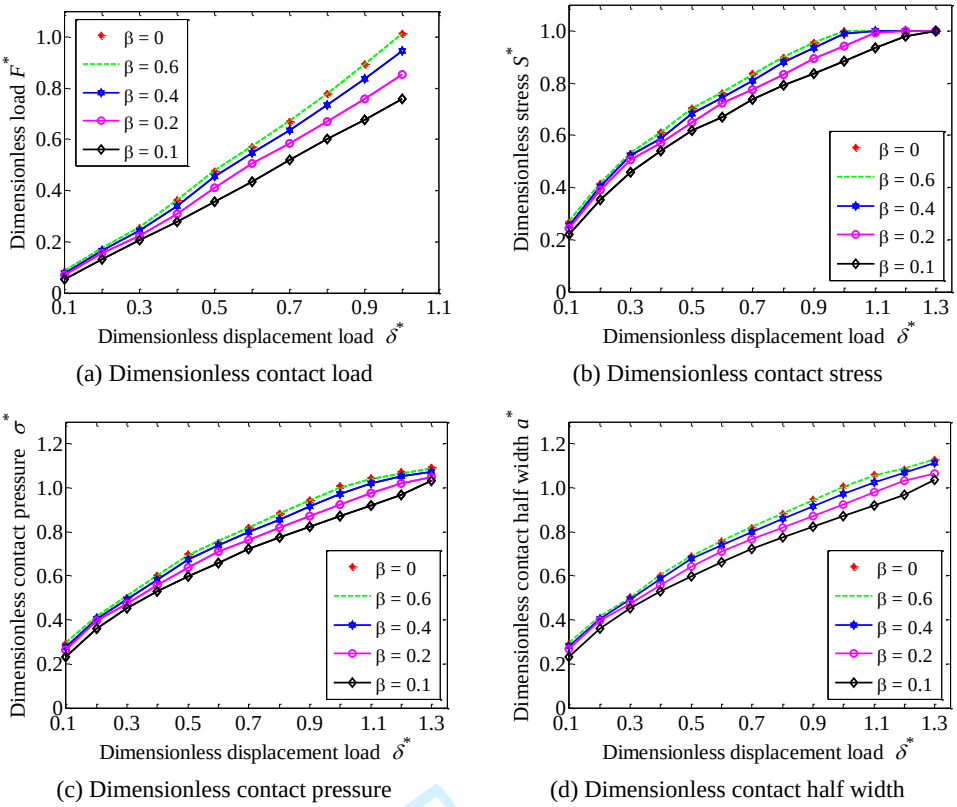

(a) Dimensionless contact load (b) Dimensionless contact stress

(c) Dimensionless contact pressure (d) Dimensionless contact half width

Figure 6: *Relationship curves of dimensionless contact parameters with dimensionless displacement loads at different peak distances in elastic contact stage*

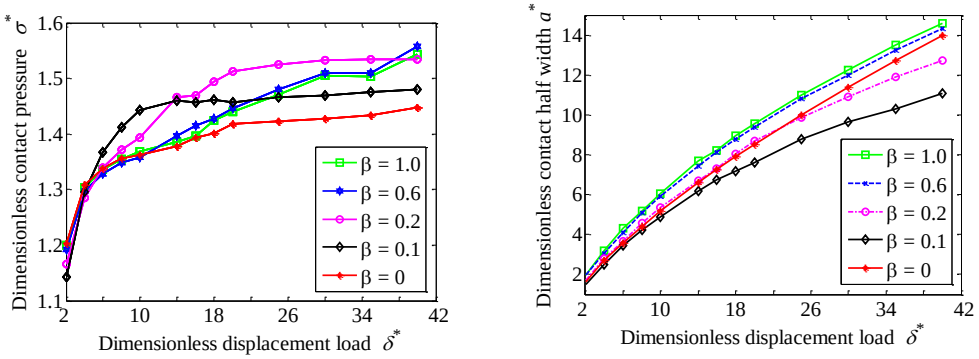

(a) Dimensionless contact pressure (b) Dimensionless contact half width

Figure 7: *Relationship between dimensionless contact parameters and dimensionless displacement load in elastoplastic contact stage*

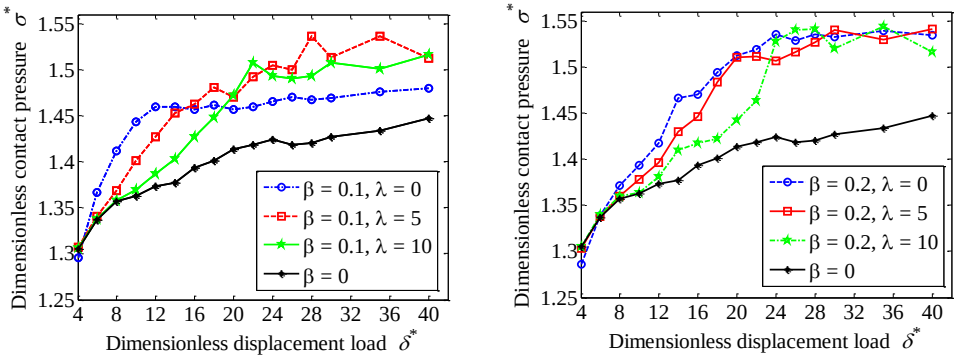

(a) β =0.1 (b) β =0.2

Figure 8: *Relationship diagrams between σ^* and δ^* of double cylindrical asperities with unequal height and different peak distance in elastoplastic contact stage*

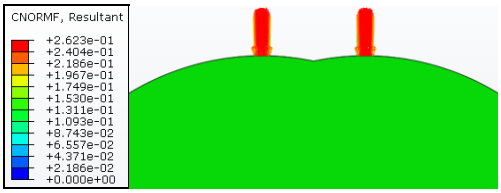

Figure 9: *Normal contact force vector of the double cylindrical asperities* (β=0.4、δ^*=10)

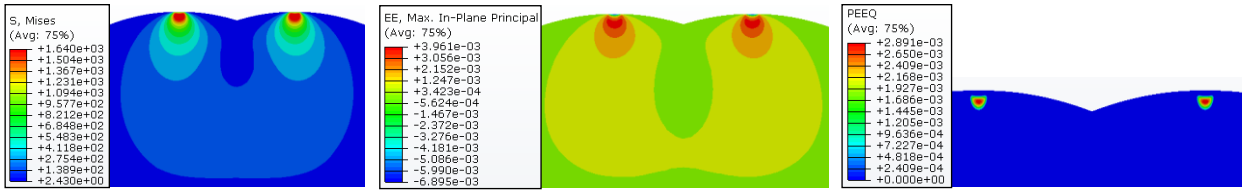

(a) Stress (b) Elastic strain (c) Plastic strain

Figure 10: *Elastoplastic contact stress contours and strain contours of the double cylindrical asperities* (β=0.6、δ^*=20)

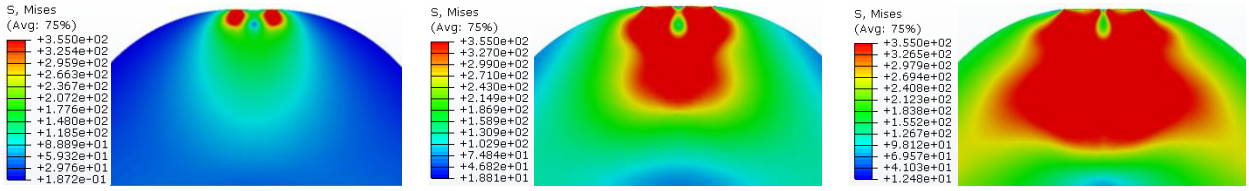

(a) δ^*=10 (b) δ^*=40 (c) δ^*=80

Figure 11: *Elastoplastic contact stress contours of the double cylindrical asperities with equal height (β=0.2)*

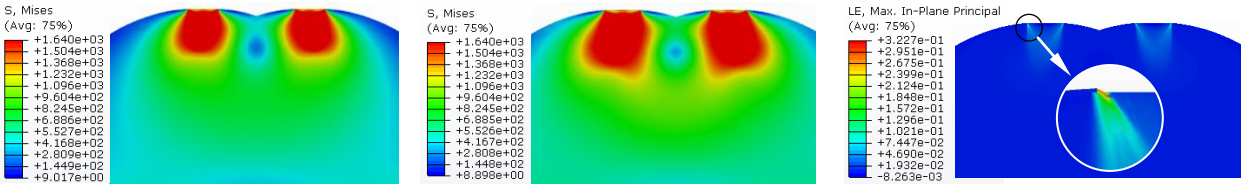

(a) Stress, δ^*=80 (b) Stress, δ^*=110 (c) Strain, δ^*=110

Figure 12. *Contact stress and strain contours of the double cylindrical asperities with equal height (β=0.6)*